**Biomechanics and Modeling in Mechanobiology manuscript No.**
(will be inserted by the editor)

# Investigating the reference domain influence in personalised models of cardiac mechanics

## Effect of unloaded geometry on cardiac biomechanics

**Myrianthi Hadjicharalambous[1,*], Christian T. Stoeck[2], Miriam Weisskopf[3], · Nikola Cesarovic[4,5,3], Eleftherios Ioannou[1], Vasileios Vavourakis[1,6,**], · David A. Nordsletten[7,8,**]**

Received: date / Accepted: date

**Abstract** A major concern in personalised models of heart mechanics is the unknown zero-pressure domain, a prerequisite for accurately predicting cardiac biomechanics. As the reference configuration cannot be captured by clinical data, studies often employ in-vivo frames which are unlikely to correspond to unloaded geometries. Alternatively, zero-pressure domain is approximated through inverse methodologies, which, however, entail assumptions pertaining to boundary conditions and material parameters. Both approaches are likely to introduce biases in model-derived biomechanical properties, nevertheless, quantification of these effects is unattainable without ground-truth data.

In this work, we assess the influence of the unloaded state on model-derived biomechanics, by employing an in-silico modelling framework relying on experimental data. In-vivo images are used for model personalisation, while in-situ experiments provide a reliable approximation of the myocardial reference domain, creating a unique opportunity for a validation study. Personalised whole-cycle cardiac models are developed which employ different reference domains (image-derived, inversely estimated) and are compared against ground-truth model outcomes. Our results find merit in both approaches, but also demonstrate differences in estimated biomechanical quantities such as material parameters, strains and stresses. Notably, they highlight the importance of image-driven boundary conditions accounting for the surrounding tissues' effect, in both forward and inverse biomechanical models.

**Keywords** zero-pressure domain · unloaded geometry · patient-specific modelling · inverse methodologies

M. Hadjicharalambous
Department of Mechanical & Manufacturing Engineering, University of Cyprus, Nicosia, Cyprus
E-mail: hadjicharalambous.myrianthi@ucy.ac.cy

* Corresponding author
[1]Department of Mechanical & Manufacturing Engineering, University of Cyprus, Nicosia, Cyprus
[2]Institute for Biomedical Engineering, University and ETH Zurich, Zurich, Switzerland.
[3]Center for Surgical Research, University Hospital Zurich, University of Zurich, Zurich, Switzerland
[4]Translational Cardiovascular Technologies, Department of Health Sciences and Technology, ETH Zurich, Zurich, Switzerland
[5]Department of Cardiothoracic and Vascular Surgery, German Heart Center Berlin, Berlin, Germany
[6]Department of Medical Physics & Biomedical Engineering, University College London, London, UK
[7]Division of Imaging Sciences and Biomedical Engineering, King's College London, United Kingdom
[8]Department of Biomedical Engineering and Cardiac Surgery, University of Michigan, MI, Ann Arbor, USA
**Share senior authorship

## 1 Introduction

Cardiac biomechanics has proven particularly useful for improving our understanding of heart function in health and disease, providing a quantitative framework for studying cardiac pathophysiology. Myocardial wall stress, for instance, has long been hypothesized as a contributing factor to tissue growth and remodelling, reported to rise in heart failure patients or after myocardial infarction (Holmes et al., 2005). Hypokinetic hearts with heterogeneous deformation have been associated with cardiomyopathies (Chuang et al., 2010), rendering myocardial strains a valuable biomarker. Material properties such as stiffness and contractility, are intrinsically linked to the tissue structural integrity and present abnormalities in ischemic conditions and diastolic heart failure. Accordingly, evaluating biomechanical properties on a patient-specific basis holds signifi-

cant potential to improve clinical diagnosis and identify individualised treatments.

Personalised cardiac mechanics models, combining mathematical modelling with clinical data, are becoming increasingly popular as a tool for non-invasively assessing biomechanical quantities. Latest models incorporate patient-specific geometries (Hadjicharalambous et al., 2017), microstructure (Stoeck et al., 2018) and boundary conditions (Asner et al., 2017), and employ physiologically accurate material description (Holzapfel and Ogden, 2009), providing enhanced accuracy in stress quantification. Model personalisation also enables the estimation of tissue stiffness and contractility, by fitting model outcomes to data-derived cavity volumes and pressures (Asner et al., 2015b; Costandi et al., 2006), three-dimensional tissue displacements and strains (Nasopoulou et al., 2017). Substantial progress has also been achieved in the parameter estimation process, through studies focusing on acquiring physiologically relevant parameters estimates (Hadjicharalambous et al., 2014a; Nasopoulou et al., 2017) or proposing efficient schemes for parametrisation and heterogeneous parameter distributions (Xi et al., 2011).

Despite these advances important model uncertainties still remain, with one important confounder being the unknown zero-pressure domain. Due to the physiological blood pressure in cardiac cavities and the generation of active tension during systole, the heart is continuously under load throughout the cardiac cycle, making it impossible to capture the unloaded domain by routinely acquired clinical data. A typical approach is to instead generate the reference domain based on an in-vivo image frame. Common choices are the end-systolic (Hadjicharalambous et al., 2017) or early diastolic (Pfaller et al., 2019) geometries, as they correspond to cardiac phases with the lowest endocardial pressures. These geometries are generally not stress-free but are instead associated with unknown in-vivo stress and strain fields, inevitably introducing inaccuracies in model-derived deformation, stress and material parameters. Other studies have employed inverse methodologies to acquire an approximation of the zero-pressure domain (Nordsletten et al., 2011; Nikou et al., 2016; Vavourakis et al., 2011) based on a deformed state and known loading conditions. Amongst them, iterative backward incremental schemes (Krishnamurthy et al., 2013) and inverse elastostatics approaches which reformulate the finite elasticity equations have drawn particular attention (Vavourakis et al., 2016; Rajagopal, 2007; Peirlinck et al., 2018). Inverse approaches in general, suffer from strong coupling between the estimated reference domain and the passive parameters, forcing studies to employ literature values or elaborate schemes for joint estimation (Nikou et al., 2016; Wang et al., 2020; Costandi et al., 2006). Furthermore, the uncertainties surrounding the unloaded domain extend to the boundary conditions that should be employed for its estimation, posing an additional challenge for inverse schemes.

Despite their shortcomings, these methods have shed light on the challenges associated with the selection of reference domain, and on its influence on model estimates of cardiac biomechanics. For instance, usage of an image frame as reference domain or employment of an inverse approach has led to distinct differences in stresses (Nikou et al., 2016), strains (Behdadfar et al., 2017; Kallhovd et al., 2019) and material parameters (Finsberg et al., 2018; Nikou et al., 2016), while the choice of specific image frames also impacts parameter values (Hadjicharalambous et al., 2017; Xi et al., 2013). While biomechanical model predictions are evidently impacted by the selection of zero-pressure domain, quantification of this influence is generally not possible due to the lack of suitable ground-truth data. In fact, very limited experimental data exist to describe the unloaded geometry and its relation to in-vivo known conditions, for instance, the study by Klotz *et al.* which proposes an empirical relation for unloaded state's cavity volume (Klotz et al., 2006). In the absence of experimental data on the reference geometry and its position relative to in-vivo states, evaluating the accuracy of existing inverse schemes, or determining appropriate boundary conditions would be unattainable. In parallel, without ground-truth data on the zero-pressure configuration it is infeasible to quantify the effect of selecting incorrect reference states on model-derived outcomes.

In this work, we aim to enhance our understanding of the importance of the unloaded configuration by employing a modelling framework relying on experimental data. Imaging data from in-vivo and in-situ experiments on a porcine hearts are used to offer detailed information on in-vivo behaviour of individual hearts, and more importantly, to provide a reliable approximation of the unloaded myocardial state. These novel datasets are used to personalise cardiac mechanics models using our previously developed data-model integration pipeline (Asner et al., 2015a; Hadjicharalambous et al., 2017), creating a unique opportunity for a validation study. In particular, we develop three whole-cycle cardiac models: (i) the ground-truth model, (ii) the end-systolic model and (iii) the inverse model, all employing a different geometry as their zero-pressure domains. A thorough comparative analysis between the three models is performed, allowing a quantitative assessment of the effect of the unloaded domain on fundamental biomechanical quantities. The ground-truth image of

the reference geometry also enables the evaluation of existing inverse methodologies, identifying model aspects that should be carefully considered when aiming to develop high-fidelity patient-specific applications.

## 2 Materials and Methods

This section describes the specifics of the experimental procedure and model development followed to examine the reference domain influence. Exploiting data from innovative in-vivo and in-situ experiments, three modelling scenarios were considered to elucidate the differences in model-derived indices caused by the deployment of different geometries as the model unloaded domain: (i) ***the ground-truth model***, which employs the unloaded geometry imaged in the in-situ experiment as the reference domain, (ii) ***the end-systolic model*** which uses the end-systolic frame of the in-vivo image as the reference domain and finally (iii) ***the inverse model***, which employs an inverse finite deformation approach to acquire an estimate for the unloaded geometry.

### 2.1 Experimental procedure

The experimental data used in this study are part of prospective in-vivo and in-situ experiments on a healthy porcine heart (Swiss Edelschwein breed, 50kg, female), approved by the local Committee for Experimental Animal Research (Cantonal Veterinary Office Zurich, Switzerland) under the License numbers ZH219/2016. The animal was anesthetized by intramuscular injection of Ketamine (15 mg/kg bodyweight (BW)), Azaperone (2 mg/kg BW) and Atropinsulfate (0.05 mg/kg BW). Analgesia was ensured by application of Buprenorphine (0.01 mg/kg BW). Throughout the experiment anesthesia was maintained with isoflurane (2% - 3.0%) by positive pressure ventilation with an inspired oxygen fraction (FiO2) of 100%, a tidal volume of 10 ml/kg and a positive end expiratory pressure (PEEP) of 5 cmH2O.

Imaging was performed on a clinical 1.5T Philips Achieva System (Philips Healthcare, Best, The Netherlands) with 5-channel dedicated cardiac receiver coil. The protocol consisted of CINE imaging in four (4CH), three (3CH) and two (2CH) chamber long-axis (LA) views and multi-slice two-chamber short-axis (SAX) view covering the entire heart. Imaging parameters were as follows: in-plane resolution: $1.5\times1.5\text{mm}^2$, slice thickness 8mm, number of heart phases 25 (SAX) / 50 (LA), no slices 13 (SAX) / 1 (LA). ECG electrodes (Quatrode patch, In-Vivo Corporation, Gainesville, USA) were placed onto the chest between the front limbs for retrospective cardiac gating.

During the in-vivo experiment, the pressure of the left ventricle (LV) was recorded at 2ms intervals, using a pigtail catheter inserted into the femoral artery and advanced to the LV cavity. The heart was consequently arrested by administration of an overdose of Pentobarbital (75 mg/Kg) and the imaging protocol was repeated. All images recorded post-mortem provided views of a reasonable approximation to the subject-specific unloaded myocardial domain (ground-truth reference images).

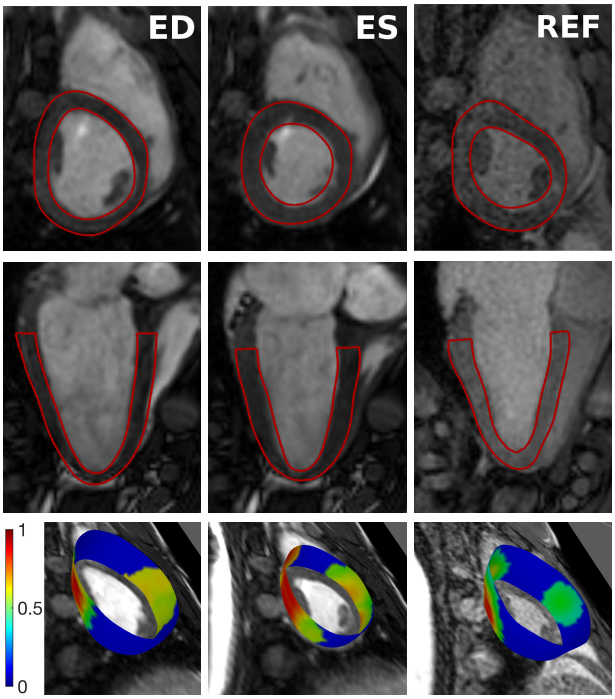


Fig. 1: CINE images of the end-diastolic (left), end-systolic (middle) and ground-truth reference (right) geometries, with the boundaries of the personalised tetrahedral meshes overlaid, in short-axis (top) and 4CH (middle) views. Bottom row demonstrates the spatial field $R$ for each mesh, which which describes the relative influence of the ribcage on the epicardial surface based on the distance between them ($R = 1$ where the epicardial surface is almost in contact with the ribcage and $R = 0$ in regions not affected by the ribcage).

### 2.2 Data processing

#### *2.2.1 Image Registration*

A critical step for model personalisation was the spatio-temporal registration of available images, to minimise misalignment due to changes in pig's position or breathing cycle. Rigid registration between the SAX and LAX

images, for both the in-vivo and reference images, was performed using MIRTK [1]. Registration of the static reference image to the dynamic in-vivo images required a more elaborate procedure, described in Appendix A.1.

#### *2.2.2 Construction of personalised FE meshes and fibre architecture*

LV meshes were constructed based on manual segmentations of the reference image, and the end-systolic (ES) and end-diastolic (ED) frames of the in-vivo images. For each case, segmentations of all LA and SAX images created with ITK-SNAP [2] (Yushkevich et al., 2006), were combined into a single mask image, which was further smoothed and truncated below the basal region. Volumetric tetrahedral meshes (Figure 1, Table 1) were then created using SimModeler [3].

To represent the anisotropic behaviour of myocardial tissue, a fibre architecture was constructed for each model. In the absence of personalised data providing insight into the microstructure on a patient-specific basis (Stoeck et al., 2014), a rule-based fibre distribution was employed (Streeter et al., 1969), consisting of circumferentially symmetric fibres, with the angle between fibres and circumferential direction varying linearly between $60^\circ$ at the endocardium and $-60^\circ$ at the epicardium.

#### *2.2.3 Data-derived displacement and pressure-volume loop*

Whole-cycle simulations for the three models were personalised using the data-derived pressure-volume loop and displacements, which were incorporated into the models through suitable boundary conditions (section 2.3.3).

Data-derived displacement $\boldsymbol{u}_d$ at ED and ES was computed by considering the reconstructed ED and ES geometries (Section 2.2.2 ) with respect to the selected reference domain for each model. The displacement for the remaining cardiac cycle was linearly interpolated. The cavity volume trace was generated using literature volume traces (Hadjicharalambous et al., 2017), scaled to the subject-specific ED and ES values. Combined with the cavity pressure measurements which were available throughout the duration of the experimental procedure, a subject-specific pressure-volume loop was generated.

[1] https://biomedia.doc.ic.ac.uk/software/mirtk/
[2] www.itksnap.org
[3] http://www.simmetrix.com/index.php/simmodeler/overview

### 2.3 Personalised cardiac mechanics model

#### *2.3.1 Kinematics and governing equations*

An indispensable part of cardiac mechanics models is the reference domain, the state of the myocardium under zero load, which is of particular interest in this work. Let $\Omega_0 \subset \mathbb{R}^3$ denote the unloaded domain with coordinates $\boldsymbol{X} \in \Omega_0$, and let the domain's boundary $\Gamma_0$ be subdivided into the basal $\Gamma_0^b$, epicardial $\Gamma_0^e$ and endocardial $\Gamma_0^\ell$ surfaces. The heart deforms continuously during the cardiac cycle, with its deformed domain $\Omega(t) \subset \mathbb{R}^3$ characterised by the physical coordinates $\boldsymbol{x} \in \Omega(t)$, for each time $t > 0$, expressed as $\boldsymbol{x} = \boldsymbol{X} + \boldsymbol{u}$, $\boldsymbol{u}$ being the tissue displacement. The deformation gradient, defined as $\boldsymbol{F} = \nabla_{\boldsymbol{X}}\boldsymbol{u} + \boldsymbol{I}$, is used to relate points in the deformed state to their reference configuration, while its determinant $J$ is used to enforce the incompressibility constraint ($J = 1$). Other kinematic quantities of interest are the right Cauchy-Green tensor $\boldsymbol{C} = \boldsymbol{F}^T\boldsymbol{F}$ and its material invariants $I_C = \boldsymbol{C} : \boldsymbol{I}$ and $I_{C_f} = \mathbf{f_0} \cdot (\boldsymbol{C}\mathbf{f_0})$ (Holzapfel and Ogden, 2009), with $\mathbf{f_0}$ denoting the fibre direction throughout the domain.

For the models considered the total potential energy $\Pi$ of the heart is given as a sum of its internal and external energies (Asner et al., 2015a), $\Pi(\boldsymbol{u}, p, \boldsymbol{\lambda}) = \Pi_{int}(\boldsymbol{u}, p) + \Pi_{ext}(\boldsymbol{u}, \boldsymbol{\lambda})$, with $\Pi_{int}$ determined by material properties and $\Pi_{ext}$ depending on external forces introduced through boundary conditions. Here $p$ and $\boldsymbol{\lambda}$ denote the hydrostatic pressure and boundary Lagrange multipliers respectively (see section 2.3.3). Based on the principle of stationary potential energy (Bonet and Wood, 2008), the primary variables $(\boldsymbol{u}, p, \boldsymbol{\lambda})$ are determined as the saddle-point solution of the potential energy:

$$\Pi(\boldsymbol{u}, p, \boldsymbol{\lambda}) = \inf_{\boldsymbol{v} \in U} \sup_{(q \times \boldsymbol{\mu}) \in W \times \Lambda} \Pi(\boldsymbol{v}, q, \boldsymbol{\mu}), \tag{1}$$

minimising the internal energy of the myocardium, while ensuring adherence to the incompressibility and boundary constraints. Here, $U \times W \times \Lambda$ denote suitable Sobolev function spaces (Asner et al., 2017).

#### *2.3.2 Constitutive laws*

In the models considered, the myocardium is treated as an incompressible, hyperelastic material, with its internal energy described as a sum of passive ($W_p$) and active ($W_a$) strain energy functions:

$$\Pi_{int}(\boldsymbol{u}, p) = \int_{\Omega_0} W_p(\boldsymbol{u}) + W_a(\boldsymbol{u}) + p(J-1)dV. \tag{2}$$

Table 1: Geometrical features of the computational domain for each model. Of interest are also the cavity volume of the estimated inverse domain $\Omega_{INV}$ (44.29mL) and the Klotz estimate (44.27mL). Characteristics of computational meshes are also presented with LNodes and QNodes denoting the number of quadratic nodes. Here $h$ is the mesh size, computed as $h = \det(\boldsymbol{S})^{1/3}$, with $\boldsymbol{S}$ the affine mapping between elements in mesh and the unit right tetrahedron. $q$ is the element quality, calculated as three times the ratio of inradius to circumradius.

| Mesh | Ground-truth | End-systolic | End-diastolic |
|---|---|---|---|
| Cavity Volume (mL) | 45.80 | 41.13 | 81.98 |
| Wall Volume (mL) | 72.3 | 71.1 | 74.5 |
| Long-axis (cm) | 6.6 | 6.3 | 7.2 |
| Short-axis (cm) | 6.2 | 5.4 | 5.8 |
| Elements | 24,320 | 23,564 | 30,496 |
| LNodes | 5,391 | 5,189 | 6,810 |
| QNodes | 37,664 | 36,358 | 47,307 |
| $h\pm$ STD($h$) (mm) | $2.57 \pm 0.39$ | $2.57 \pm 0.39$ | $2.39 \pm 0.37$ |
| $q\pm$ STD($q$) (mm) | $0.77 \pm 0.10$ | $0.78 \pm 0.10$ | $0.77 \pm 0.11$ |

Material laws were selected to combine physiologically accurate myocardial function with good parameter identifiability characteristics (Hadjicharalambous et al., 2014a; Asner et al., 2015a) . In particular, a reduced form of the Holzapfel-Ogden law (Holzapfel and Ogden, 2009) was employed:

$$\begin{aligned} W_p(\boldsymbol{u}) =& \frac{a}{2b}\left(\exp[b(I_C-3)]-1\right) \\ &+ \frac{a_f}{2b_f}\left(\exp[b_f(I_{C_f}-1)^2]-1\right), \end{aligned} \tag{3}$$

with $a$ characterising the bulk tissue stiffness and $a_f$ the stiffness along the fibre direction. The exponents $b$ and $b_f$ which affect the nonlinear tissue response, were kept constant throughout simulations ($b = 5$, $b_f = 5$) (Hadjicharalambous et al., 2014a).

The active behaviour was described with a law entailing a single, time-dependent, contractility parameter $\alpha(t)$:

$$W_a(\boldsymbol{u}) = \alpha(t)\phi_{iso}(\boldsymbol{u}). \tag{4}$$

Here $\phi_{iso}(\boldsymbol{u})$ describes the dependence of activation on cell length (Kerckhoffs et al., 2003), and enables isotropic activation near the apical region to avoid known singularities (Asner et al., 2017).

### *2.3.3 Boundary conditions*

Selecting boundary conditions is a critical step in model development, as they provide a means of representing the individual loads affecting the heart's surface and can incorporate data-derived motion into the model. Boundary conditions were introduced through boundary energies, using Lagrange multipliers:

$$\Pi_{ext}(\boldsymbol{u}, \boldsymbol{\lambda}) = \sum_{k\in(b,\ell,e)} \Pi^k_{ext}(\boldsymbol{u}, \boldsymbol{\lambda}_k). \tag{5}$$

Whole-cycle simulations were driven using cavity volumes, whereby the mesh lumen volume $V(t)$ was set equal to the data-derived volume trace $V_d(t)$ at each timestep:

$$\Pi^\ell_{ext} = \lambda_\ell(V(t) - V_d(t)). \tag{6}$$

In this setting, $\lambda_\ell$ acts as the cavity pressure (Asner et al., 2015b, 2017).

For the basal boundary, a relaxed boundary condition was used to avoid strict adherence to noisy data and limit non-physiological stress peaks associated with Dirichlet conditions (Asner et al., 2017):

$$\Pi^b_{ext} = \int_{\Gamma^b_0} \boldsymbol{\lambda}_b \cdot (\boldsymbol{u} - \boldsymbol{u}_d - \frac{\epsilon_b}{2}\boldsymbol{K}_b\boldsymbol{\lambda}_b)\ \ dA. \tag{7}$$

Here $\boldsymbol{K}_b = \boldsymbol{I} - \boldsymbol{n}_b(t)\otimes\boldsymbol{n}_b(t)$ is a penalty matrix, which forces displacements along the base normal vector $\boldsymbol{n}_b$ to be equivalent to data, while allowing a relaxed adherence through the base plane. The penalty parameter $\epsilon_b$ ($0 < \epsilon_b \ll 1$) controls the degree of enforcement of the constraint, depending on data quality or numerical considerations.

In terms of epicardial boundary conditions, the zero external energy ($\Pi^e_{ext} = 0$) was considered following the majority of studies. However, the heart is not in isolation, but instead is surrounded by the pericardial sac and is in close proximity to the lungs, the ribcage and the diaphragm. In fact, due to the porcine anatomy, the ribcage is found particularly close to the heart, potentially affecting myocardial motion and stress fields. Therefore, additional constraints were also considered which account for the ribcage's influence on the LV, by restricting the displacement of the epicardial wall in a region adjacent to the ribcage:

$$\Pi^e_{ext} = \int_{\Gamma^e_0} \boldsymbol{\lambda}_e \cdot (R(\boldsymbol{u} - \boldsymbol{u}_d) - \frac{\epsilon_e}{2}\boldsymbol{K}_e\boldsymbol{\lambda}_e)\ \ dA. \tag{8}$$

Here $\boldsymbol{\lambda}_e$ is a Lagrange multiplier defined over the epicardial surface and $R : \Gamma^e_0 \to [0, 1]$ is a spatial field signifying the influence of the ribcage on the epicardial surface

based on their distance, as derived from the segmentations of SAX images (Figure 1). $R$ varies smoothly between 0 and 1, with 1 marking the epicardial regions most adjacent to the ribcage. The penalty matrix follows the basal boundary condition ($\boldsymbol{K}_e = \boldsymbol{I} - \boldsymbol{n}_r \otimes \boldsymbol{n}_r$), enforcing a stronger adherence of the constraint along the normal vector of the rib-adjacent ($\boldsymbol{n}_r$) region. This constraint was employed for the end-systolic and inverse models.

In the ground-truth model, however, constraints were also considered for the apical region, due to substantial variations in the positions of the reference and in-vivo domains (see Appendix A.1). The epicardial surface was further subdivided into an apical region ($\Gamma_0^e = \Gamma_0^a \cup \Gamma_0^{e\setminus a}$), to enable the restriction of perpendicular motion in the apical region:

$$\begin{aligned} \Pi_{ext}^e = w_e \int_{\Gamma_0^{e\setminus a}} \boldsymbol{\lambda}_e \cdot (R(\boldsymbol{u}-\boldsymbol{u}_d) - \frac{\epsilon_e}{2}\boldsymbol{K}_e\boldsymbol{\lambda}_e)\ dA \\ + w_a \int_{\Gamma_0^a} \boldsymbol{\lambda}_a \cdot (\boldsymbol{u}-\boldsymbol{u}_d - \frac{\epsilon_a}{2}\boldsymbol{K}_a\boldsymbol{\lambda}_a)\ dA. \end{aligned} \tag{9}$$

where $\boldsymbol{K}_a = \boldsymbol{I} - \boldsymbol{n}_a \otimes \boldsymbol{n}_a$, with $\boldsymbol{n}_a$ the normal vector to the apical region. The scalars $w_e$ and $w_a$ were either 0 or 1, allowing for selective enforcement of the two epicardial constraints, leading to the following combinations of boundary conditions for the ground-truth model:

- B: Only basal boundary condition while $\Pi_{ext}^e = 0$ ($w_e = 0$, $w_a = 0$),
- BA: Data-derived deformation prescribed on basal and apical regions ($w_e = 0$, $w_a = 1$),
- BR: Data-derived deformation prescribed on basal plane, restricted motion in ribcage-adjacent region ($w_e = 1$, $w_a = 0$),
- BAR: Prescribed deformation on basal and apical regions and restricted motion near the ribcage ($w_e = 1$, $w_a = 1$).

### *2.3.4 Parameter estimation*

For the ground-truth and end-systolic models, passive material parameters were estimated by minimising the error between the simulated ED state for each model and the in-vivo ED geometry. Three error metrics were considered, namely the root mean square error (RMSE), and the mean and maximum distance errors ($d_{mean}$ and $d_{max}$). Error metrics were calculated with respect to nodal distances between the simulated ED mesh ($\boldsymbol{x}_{ED}^{sim}$) for each model and the data-derived ED mesh ($\boldsymbol{x}_{ED}$):

$$\begin{aligned} &d_i = \min_j ||\boldsymbol{x}_{ED}^{sim}(i) - \boldsymbol{x}_{ED}(j)||, \quad RMSE = \sqrt{\frac{\sum_i d_i^2}{N_n}}, \\ &d_{mean} = \frac{\sum_i d_i}{N_n}, \quad d_{max} = \max_i d_i. \end{aligned} \tag{10}$$

Here $d_i$ represents the distance of node $i$ of the simulated ED mesh to the closest node in the data-derived ED mesh, and $N_n$ is the total number of nodes for the former mesh.

As previously described (Asner et al., 2015a), passive parameters $a$ and $a_f$ can be estimated by initially reducing the parameter space to only the parameter ratio $a/a_f$. The ratio was estimated through parameter sweeps and considering aforementioned error metrics, by keeping $a_f^{sim}$ constant and varying $a^{sim}$. The absolute values of both parameters were then retrieved by scaling by the ratio between the data-derived ED pressure $P^{ED}$ and its simulated value $\lambda_\ell^{sim}$:

$$a = a^{sim}\frac{P^{ED}}{\lambda_\ell^{sim}}, \qquad a_f = a_f^{sim}\frac{P^{ED}}{\lambda_\ell^{sim}}. \tag{11}$$

The described estimation process was however not appropriate for the inverse model. Reference domain estimation is directly dependent on the material parameters, which in turn, require an assumed unloaded domain for quantification. To circumvent this coupling, the reference domain and material parameters were jointly estimated using sweeps over passive parameters and inverse simulations. A cavity volume error metric $V_d^{ref}$ was used for estimation, defined as the difference between the cavity volume of the simulated reference domain $V_{(a,a_f)}^{ref}$ and its Klotz estimate ($V_{Klotz}^{ref} = 44.27$mL):

$$V_d^{ref} = |V_{(a,a_f)}^{ref} - V_{Klotz}^{ref}|. \tag{12}$$

However, it was impossible to uniquely identify both passive parameters using only estimation by cavity volumes (Appendix A.2). To circumvent this, a combination of existing schemes (Nikou et al., 2016; Xi et al., 2013) was used, whereby the end-systolic frame provided an initial guess for the zero-pressure geometry, and an initial estimate of passive parameters was acquired through forward simulations (*i.e.*, these coincide with parameters estimated for the end-systolic model). Subsequently, inverse simulations with parameter sweeps were run, whereby $a_f$ was set to its initial estimate and $a$ was allowed to vary. The new estimate of the reference domain $\Omega_{INV}$ and $a$ were then obtained by minimising $V_d^{ref}$.

Finally, once passive characteristics were configured, active tension for all models was estimated by matching cavity pressures. The scaling $\alpha$ of the active tension in Eq. 4 was estimated at each timestep, by minimising the absolute difference $P_d$ between data-derived and simulated LV pressures ($P_d(t) = |P(t) - \lambda_\ell(t)|$).

#### *2.3.5 Numerical Solution*

Biomechanical models were solved using a standard Galerkin FE scheme. Displacement and hydrostatic pressure variables were interpolated using quadratic and linear tetrahedral elements respectively, to ensure the mixed formulation's stability (Hadjicharalambous et al., 2014b), while quadratic triangular elements were used for epicardial and basal multipliers. All numerical problems were solved using **$\mathcal{C}$Heart**, a multiphysics FE solver (Lee et al., 2016).

### 2.4 Three model scenarios of full-cycle biomechanics

#### *2.4.1 Ground-truth model ($\Omega_0 = \Omega_{REF}$)*

In the ground-truth scenario, the model reference domain was provided by the MR image of the unloaded myocardial configuration (section 2.1). To simulate the passive mechanics, the reference domain was inflated to the ED cavity volume, through Eq. 6. In terms of basal and epicardial boundary conditions, numerous perturbations of Eq. 7-9 were considered, to identify a combination able to sufficiently match the ED geometry. Passive and active parameters were evaluated as described in Section 2.3.4 allowing for full-cycle simulations.

#### *2.4.2 End-systolic model ($\Omega_0 = \Omega_{ES}$)*

For this model scenario, the segmentation of the ES image provided the unloaded domain. Base displacements were prescribed through Eq. 7, while deformation in the region adjacent to the ribcage was constrained through Eq. 8.

#### *2.4.3 Inverse model ($\Omega_0 = \Omega_{INV}$)*

The final model scenario employed an inverse methodology to estimate the unloaded domain. The aim was to evaluate the influence of inverse approaches on model outcomes, therefore, any information derived from the ground-truth reference image was ignored. Model personalisation was thus performed based only on cavity pressures $P(t)$, ED geometry and $V_{Klotz}$.

The basal surface was kept constrained, as is common in most inverse cardiac models (Eq. 7, $\boldsymbol{u}_d = 0$). Two constraints were considered for the epicardial surface: a zero-traction condition, used almost exclusively in inverse cardiac mechanics applications, and a ribcage condition restricting the deformation of the rib-adjacent epicardium (Eq. 8). $\Omega_{INV}$ was estimated using the approach of Rajagopal *et al.*, whereby the Jacobian matrix is computed with respect to reference state parameters (Rajagopal, 2007). Joint estimation of $\Omega_{INV}$ and passive parameters was performed as described in Section 2.3.4, followed by active tension estimation.

## 3 Results

### 3.1 Assessment of boundary conditions

#### *3.1.1 Boundary conditions for the ground-truth model*

Several combinations of epicardial and basal boundary conditions (Section 2.3.3), along with perturbations of relaxation parameters ($\epsilon_b$, $\epsilon_e$ and $\epsilon_a$) were considered for the ground-truth model. The suitability of each combination was assessed using the distance error metrics in Section 2.3.4. A representative illustration of perturbations of relaxation parameters is depicted in Figure 2, when the BAR boundary condition was employed. Good identifiability characteristics were observed for each error metric, with a unique minimum in each case. Notably, the combinations of ($\epsilon_b$, $\epsilon_e$) providing minimum errors were similar in all three metrics, suggesting that ($\epsilon_b = 5e-6$, $\epsilon_e = 5e-7$) would provide a reasonable choice.

Figure 3 illustrates the overall effect of the employed combination of boundary conditions on model accuracy. For all error metrics, the maximum value was observed when only the basal boundary condition was employed, while the introduction of the apical constraint caused a substantial reduction. The decrease in error was even more striking when the ribcage condition was employed, leading to a more than 50% reduction in the maximum error.

#### *3.1.2 Boundary conditions for the end-systolic model*

The choice of boundary conditions was also examined for the case of a data-derived geometry employed as the reference domain. Several combinations of relaxation parameters $\epsilon_b$ and $\epsilon_e$ were run, with the combination ($\epsilon_b = 1e-6$, $\epsilon_e = 5e-6$) found to produce consistently good results across three error metrics (Figure 2).

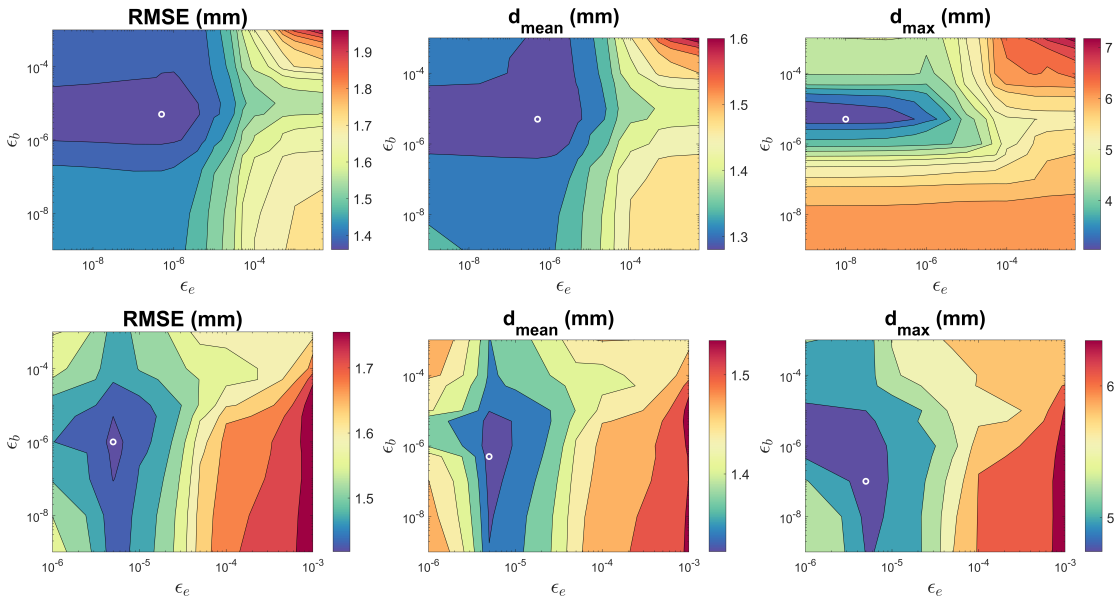


Fig. 2: Distance error metrics for varying values of the relaxation parameters $\epsilon_b$ and $\epsilon_e$ in diastolic simulations of the reference model using BAR with $\epsilon_a = 1e-7$ (top) and of the end-systolic model (bottom). White circles depict the combination ($\epsilon_b$, $\epsilon_e$) providing the lowest error for each error metric.

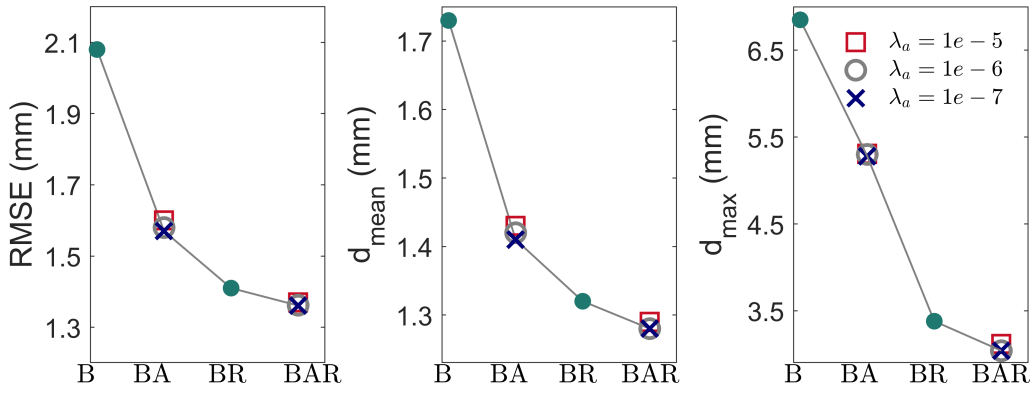


Fig. 3: Error metrics for each combination of boundary conditions over LV inflation simulations of the ground-truth model. For each combination, the error corresponds to the lowest value achieved with respect to the relaxation parameters $\epsilon_b$ and $\epsilon_e$.

### *3.1.3 Boundary conditions for the inverse model*

Numerous perturbations were also considered for the inverse model to investigate the suitability of boundary conditions. Those accounting for the relaxed basal boundary condition and zero epicardial energy exhibited considerable numerical issues, with the majority failing to converge to a solution. These issues were present for a wide range of $\epsilon_b$ and passive parameters, but were more pronounced for stronger enforcement of the basal constraint and softer material. Visualisations of model deformation prior to simulation failure revealed non-physiological deformation including surface bending (Figure 4).

Table 2: Estimates for the passive ($a$ and $a_f$) and maximum active $\alpha_{max}$ parameters, obtained when employing the ground truth, end-systolic and inverse models

| **Modelling scenario** | $a$ (Pa) | $a_f$ (Pa) | $\alpha_{max}$ (kPa) |
|---|---|---|---|
| Ground-truth model | 792 | 1200 | 125 |
| End-systolic model | 425 | 1326 | 106 |
| Inverse model | 800 | 1326 | 136 |

On the contrary, similar computational issues were not present when inverse simulations accounted for the ribcage influence on LV motion. The majority of these simulations run without any issues, for many combinations of passive parameters, providing reasonable reference domain estimations (Figure 4).

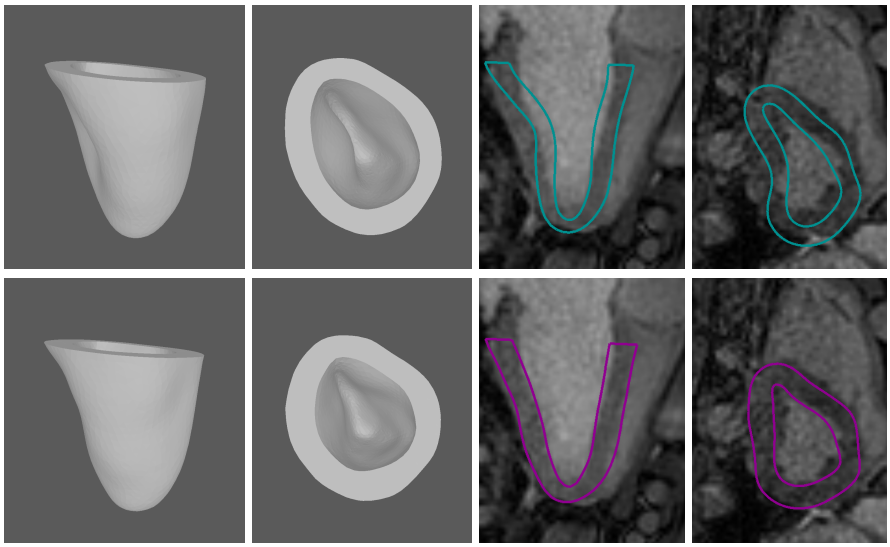

Fig. 4: Inverse simulations employing either a zero epicardial condition (top row), or an epicardial condition accounting for the influence of the ribcage on the LV wall (bottom row). Short-axis and long-axis views of the simulated inverse geometries are provided, and are overlaid onto the reference short-axis and 4-chamber views for comparisons to the actual unloaded geometry. The simulation employing a zero epicardial boundary condition (top row) failed at a cavity volume higher than $V_{Klotz}$, suggesting that even more spurious deformation modes would appear had the simulation run up to $V_{Klotz}$.

Table 3: Error metrics using the three models at end-diastole and at end-systole. RMSE, $d_{mean}$ and $d_{max}$ correspond to nodal distance metrics between meshes. $D$ denotes the Dice similarity coefficient, computed over mask images generated from the model-derived and image-derived ED and ES geometries.

| Model | Ground-truth | End-systolic | Inverse |
|---|---|---|---|
| At end-diastole | | | |
| RMSE (mm) | 1.36 | 1.40 | 0.23 |
| $d_{mean}$ (mm) | 1.28 | 1.31 | 0.21 |
| $d_{max}$ (mm) | 3.15 | 4.89 | 0.61 |
| D | 0.82 | 0.79 | 0.97 |
| At end-systole | | | |
| RMSE (mm) | 1.56 | 1.38 | 1.55 |
| $d_{mean}$ (mm) | 1.44 | 1.30 | 1.42 |
| $d_{max}$ (mm) | 6.45 | 4.07 | 5.61 |
| D | 0.85 | 0.90 | 0.85 |

### 3.2 Comparison of passive parameters

For the ground-truth and end-systolic models, parameter estimation was performed through parameter sweeps (Section 2.3.4). Simulations with varying values of the isotropic parameter were run ($a^{sim} \in [50, 2000]Pa$), while the fibre parameter was set ($a_f^{sim} = 1kPa$). Absolute values of $a$ and $a_f$ are provided in Table 2, while the errors achieved for the estimated parameters for each model are presented in Table 3.

For the inverse model, joint estimation of passive parameters and reference domain was performed. The fibre parameter was set to its initial estimate ($a_f = 1326$ Pa) and only the isotropic parameter was allowed to vary ($a^{sim} \in [50, 2000]Pa$). A unique minimum was observed in this case, leading to the passive parameters in Table 2, and to the estimated reference domain depicted in Figure 4.

### 3.3 Comparison of estimated active tension

Active mechanics were characterised following the procedure in Section 2.4.1. Parameter sweeps were performed for each timestep, with $\alpha(t)$ varying between $[0, 150]$ kPa. For all modelling scenarios, a unique minimum of the pressure error was achieved for each timestep. Estimated active tension curves are depicted in Figure 5, maximum values are presented in Table 2, while the agreement with the ES geometry is assessed in Table 3.

### 3.4 Comparison of stresses and strains

For each modelling scenario, full-cycle simulations employing the estimated passive and active parameters were run. The Cauchy stress and Green-Lagrange strain along the fibre direction were computed, both at ED and ED. Average values are presented in Table 4, while their spatial distrubutions are illustrated in Figures 6 and 7.

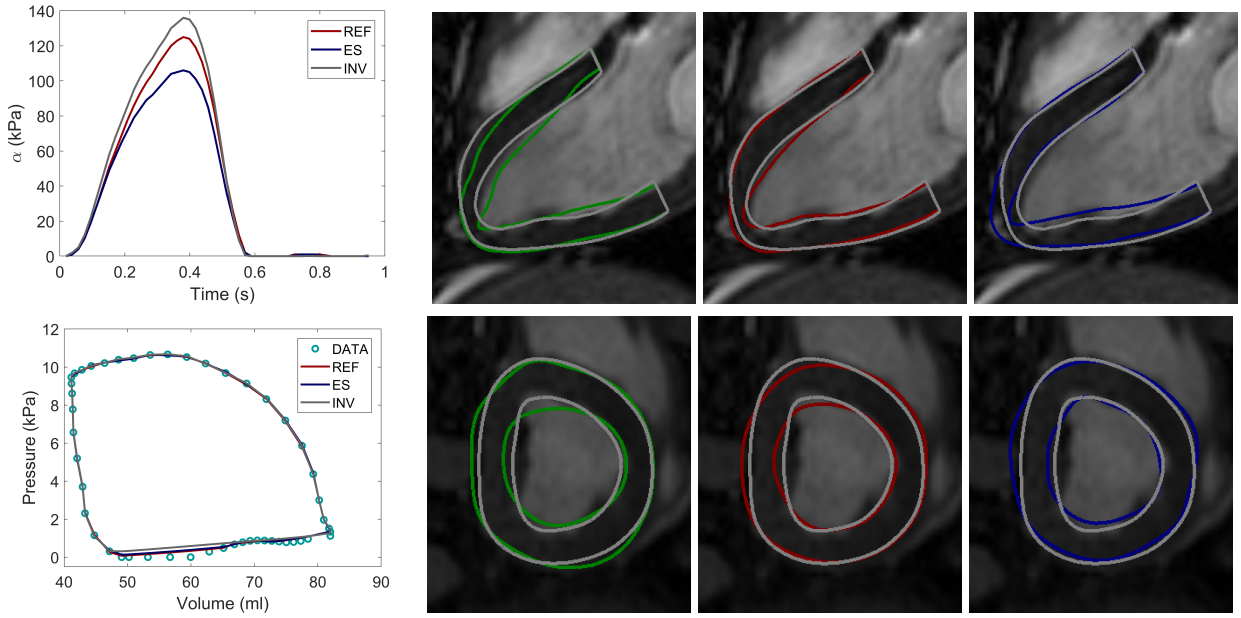


Fig. 5: (Left, top) Estimated active tension and (left, bottom) simulated pressure-volume loops for the three models, compared against the data-derived pressure-volume loop. 3-chamber (right, top row) and short-axis (right, bottom row) view of end-systolic image, with overlaid the end-systolic mesh (in white) and the simulated end-systolic geometries when employing the ground-truth (in green), end-systolic (in red) and inversely estimated (in blue) unloaded domains.

Table 4: Mean values of Cauchy fibre stress $\boldsymbol{\sigma}_f$ and Green-Lagrange fibre strain $\boldsymbol{E}_f$ with each model, at ED and ES.

| | Ground-truth | End-systolic | Inverse |
|---|---|---|---|
| ED $\boldsymbol{\sigma}_f$ (kPa) | 2.81 | 4.32 | 2.22 |
| ES $\boldsymbol{\sigma}_f$ (kPa) | 23.48 | 23.46 | 22.28 |
| ED $\boldsymbol{E}_f$ | 0.14 | 0.17 | 0.13 |
| ES $\boldsymbol{E}_f$ | -0.04 | -0.06 | -0.07 |

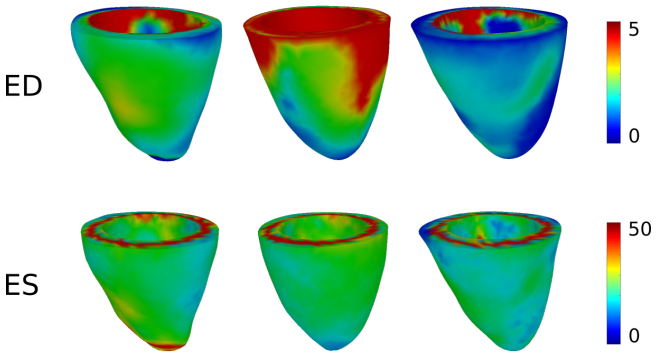


Fig. 6: Cauchy stress (kPa) in the fibre direction at ED (top row) and ES (bottom row), for the reference (left), the end-systolic (middle) and the inverse (right) models.

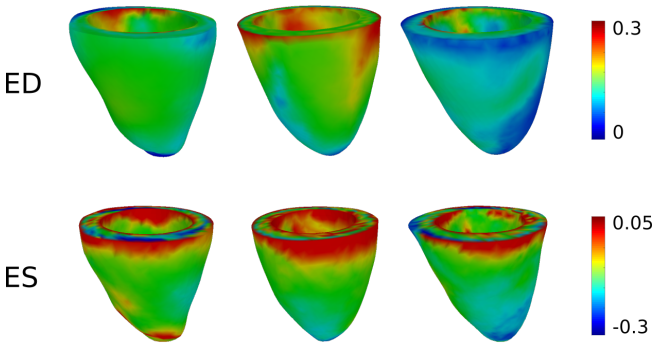


Fig. 7: Green-Lagrance strain in the fibre direction at ED (top row) and ES (bottom row), for the reference (left), the end-systolic (middle) and the inverse (right) models.

## 4 Discussion

### 4.1 Assessment of boundary conditions

Exploiting the invaluable data on the myocardial reference domain and its relation to in-vivo geometries, we were able to develop a computational framework for reliable forward and inverse simulations, transitioning between the unloaded and ED domains. Error quantification revealed the importance of accounting for the surrounding tissues, with a remarkable improvement in model errors reported when the ribcage boundary condition was employed for all models. Importantly, inverse simulations employing only a basal constraint exhibited numerical issues and predicted geometrical abnormalities, suggesting that the ribcage constraint was not only

important for model accuracy, but also necessary for simulation convergence.

The ribcage constraint led to more than 50% reduction in errors, while errors were lowest when all constraints were enforced. While this is not surprising as larger parts of the geometry were penalised, the relative impact of constraints is interesting. Inclusion of the apical constraint resulted in improved agreement with the data-derived geometries, yet this effect was not as critical as neglecting the ribcage influence which led to non-physiological cardiac deformations, penetrating the ribcage surface.

### 4.2 Influence of reference domain on model outcomes

The employed reference domain was shown to affect passive parameter quantification. Estimates obtained with the end-systolic model suggested more anisotropic material properties compared to ground-truth and inverse models, in agreement with earlier studies *et al.* (Nikou et al., 2016). The parameters estimated within the inverse framework were in better agreement with the ground-truth parameters, nevertheless, their values are not unique and depend on the joint estimation scheme employed (Appendix A.2). Despite variations between models, passive parameters were of the same order of magnitude. For comparison, $a$ and $a_f$ exhibited five-fold increase in patients with dilated cardiomyopathy compared to healthy volunteers (Hadjicharalambous et al., 2017). Therefore, while the reference domain influences the absolute parameter values, the correct order of magnitude was captured by all three models. Notably, all models were able to capture the data-derived diastolic part of the cycle, with satisfactory agreement to the ED geometry and pressure-volume loop.

The unloaded domain had little qualitative effect on active characteristics, with active tension curves following the same temporal evolution. However, quantitative differences of 15.2% and 8.8% were observed in $\alpha_{max}$ for the end-systolic and inverse models respectively. Although active tension estimation neglected any displacement observations, there was a fair agreement between the simulated and data-derived ES geometries, for all cases. Notably, despite differences in the estimated active tension, all modelling scenarios were able to reproduce the pressure-volume loop, suggesting that such gross metrics are insensitive to the selection of reference domain

Substantial variations were observed in ED stresses. The end-systolic model gave higher ED stresses, in agreement with previous studies reporting lower ED stresses when an unloading algorithm was employed (Nikou et al., 2016). Apart from geometrical discrepancies in the employed reference configurations, the different passive parameters of the three models might contribute to ED stresses' variations, as passive parameters have a significant correlation with ED stresses (Behdadfar et al., 2017). On the contrary, ES stresses did not vary markedly in the three modelling scenarios, with both the global average values and their spatial distributions showing considerable similarities.

ED strains presented similar spatial patterns, particularly between the ground-truth and inverse models. The end-systolic model exhibited larger average and maximum values, potentially due to its larger cavity volume difference to the ES mesh. End-systolic stains presented very similar spatial distributions, suggesting their insensitivity to the employed reference domain.

Notably, the variations in model outcomes resulted from reference domains with very similar cavity and wall volumes (Table 1), highlighting the importance of incorporating patient-specific geometries and boundary conditions.

### 4.3 Evaluation of common choices for the unknown reference domain

Usage of in-vivo frames as the unloaded configuration has been very popular in cardiac mechanics, due to its ease in implementation using routinely-acquired data and low computational cost compared to inverse schemes. Based on the conclusions of this study, employing the ES geometry as the reference domain could be a reasonable choice when quantities such as pressure-volume loops and ES stresses and strains are of interest, as these are relatively insensitive to the choice of unloaded domain. However, studies focusing on ED strains or estimated stiffness and contractility parameters – which presented variation from ground-truth values – would need to take into account the potential inaccuracies caused by employing a data frame as reference. Nevertheless, the end-systolic model – which can easily be generated from in-vivo data – holds potential for clinical utility, particularly in cases where a disease causes major variations in these quantities or when any bias induced is reproducible across patients in a disease cohort.

Alternatively, inverse methodologies have been employed in many cardiac mechanics models to provide an unloaded domain. The approach followed within led to a reference estimate with a cavity volume very close to the ES frame (Table 1), yet very different geometries (see Figures 1 and 4), which in turn resulted in substantial variations in results. The passive and active parameters along with ED stresses obtained with the inverse

model were in closer agreement with ground-truth values, compared to the end-systolic model. Studies interested in such quantities – which appear to be sensitive to the choice of reference domain – might consider an inverse approach, by weighing the benefit of enhanced accuracy over the additional computational cost. Nevertheless, care should be taken in the selection of appropriate basal and epicardial boundary conditions as these are critical for the accuracy of the inverse methodology.

### 4.4 Study limitations

The experimental procedure followed enabled us to reliably capture the heart's unloaded domain, creating a unique opportunity for quantitatively assessing its influence on model outcomes. However, the pressure in the post-mortem setting was probably non-zero and was likely equal to venous pressure, which would exert load in the myocardium – albeit much lower than in-vivo. Due to the animal's positioning, additional loading stems from gravity which is also likely to induce deformation in our imaged reference domain. However, this effect should be similar in the in-vivo images and is thus unlikely to affect the comparative analysis.

Furthermore, despite many iterative schemes for the joint estimation of the reference domain and material parameters, only one approach was considered herein. The evaluation of the current approach was valuable in highlighting important aspects to consider when running inverse simulations, the numerical difficulties associated with inverse simulations, and more importantly the necessity for choosing suitable boundary conditions. The specific joint estimation scheme employed might had introduced additional uncertainty. While the ground-truth and end-systolic models should provide unique passive parameters (Hadjicharalambous et al., 2014a), parameter uniqueness can not be guaranteed for the inverse model, whereby an almost arbitrary value was selected for $a_f$. Nevertheless, different passive parameters (Appendix A.2) led to similar active tension, stresses and strains, suggesting that our conclusions would hold for similar schemes.

Parameter estimates are also affected by the boundary conditions employed (Hadjicharalambous et al., 2017). This dependence was observed in the passive estimates of the ground-truth model with different basal constraints (Appendix A.2) nonetheless, the effect on active tension was less pronounced. Boundary conditions are also likely to affect stress and strain fields, both directly and indirectly through their influence on passive parameters. Nevertheless, similar boundary conditions were employed in all models, enabling reliable comparisons. Additional boundary conditions could also be considered in the future, to account, for instance, for the effect of the right ventricle on the LV, which is expected to be substantial (Hadjicharalambous et al., 2017).

LV cavity pressure measurements, which were available throughout the experimental procedure, had consistently high end-diastolic and low end-systolic values. This suggested the presence of a systematic error, potentially caused by inaccurate positioning of the pressure catheter relative to the heart or by the anesthetic administered. To avoid discarding the entire dataset, the pressure curve was scaled to achieve physiological porcine end-diastolic and end-systolic LV pressures (Kolipaka et al., 2010), thus retaining personalised temporal information and relative pressures through the cycle.

Additionally, residual stresses due to growth and remodelling were ignored, even though they were likely present in the myocardium throughout the cardiac cycle and at its unloaded state. Considering the challenge of experimentally measuring and accurately modelling residual stresses, this study focused on the effect of the unloaded domain. Nevertheless, understanding the influence of residual stresses on reference domain and model outcomes would be a valuable future development.

Finally, the conclusions of this study stem from a porcine subject. While direct extrapolation to human hearts cannot be guaranteed, important similarities in cardiac function between the two species suggest that similar conclusions might hold for humans. Importantly, these experiments – which would not had been possible on humans – enabled a thorough analysis of common choices for unloaded domain, and a systematic assessment of their influence on model biomechanics.

## 5 Conclusions

This work deals with a major limitation in models of cardiac mechanics, namely the unknown reference domain. Exploiting ground-truth data from in-vivo and in-situ experiments on a porcine heart, this study has employed an in-silico modelling framework to quantitatively assess the effect of the unloaded domain on model-derived biomechanics. Personalised whole-cycle cardiac models were developed, employing common approaches for selecting the reference domain (image-derived, inversely estimated), and were systematically compared against ground-truth data. Our results give credit to both approaches, but also elucidate important discrepancies in their estimates of material parameters, stresses and strains, during both the passive and

active phase of the cardiac cycle. Notably, they draw attention to the importance of patient-specific image-driven boundary conditions, in both forward and inverse biomechanical models.

## Acknowledgments

This is a preprint of an article published in Biomechanics and Modeling in Mechanobiology. The final authenticated version is available online at: https://doi.org/10.1007/s10237-021-01464-2. The authors would like to acknowledge funding from the University of Cyprus. D.N. would like to acknowledge funding from Engineering and Physical Sciences Research Council (EP/N011554/1 and EP/R003866/1). CTS would like to acknowledge funding from Swiss national science foundation (PZ00P2_174144 ).

## Declarations

### Funding

Financial support was received from the University of Cyprus, the Engineering and Physical Sciences Research Council (EP/N011554/1 and EP/R003866/1) and from Swiss national science foundation (PZ00P2 _174144).

### Conflicts of interest/Competing interests

The authors declare no conflict of interest.

### Ethics approval

The study received ethical approval by the local Committee for Experimental Animal Research (Cantonal Veterinary Office Zurich, Switzerland) under the License numbers ZH219/2016.

### Consent to participate

Not applicable

### Consent for publication

Not applicable

### Availability of data and material

Imaging data is available upon request.

### Code availability

All numerical problems were solved using $\boldsymbol{\mathcal{C}}$**Heart**(Lee et al., 2016).

## References

Asner L, Hadjicharalambous M, Chabiniok R, Peresutti D, Sammut E, Wong J, Carr-White G, Chowienczyk P, Lee J, King A, Smith N, Razavi R, Nordsletten D (2015a) Estimation of passive and active properties in the human heart using 3D tagged MRI. Biomech Model Mechanobiol pp 1–19, DOI 10.1007/s10237-015-0748-z

Asner L, Hadjicharalambous M, Lee J, Nordsletten D (2015b) STACOM Challenge: Simulating Left Ventricular Mechanics in the Canine Heart. In: Statistical atlases and computational models of the heart, pp 123–134, DOI 10.1007/978-3-642-28326-0-26

Asner L, Hadjicharalambous M, Chabiniok R, Peressutti D, Sammut E, Wong J, Carr-White G, Razavi R, King AP, Smith N, Lee J, Nordsletten D (2017) Patient-specific modeling for left ventricular mechanics using data-driven boundary energies. Comput Methods Appl Mech Eng 314:269–295, DOI 10.1016/j.cma.2016.08.002, URL http://dx.doi.org/10.1016/j.cma.2016.08.002, 1011.1669v3

Behdadfar S, Navarro L, Sundnes J, Maleckar MM, Avril S (2017) Importance of material parameters and strain energy function on the wall stresses in the left ventricle. Comput Method Biomec 20(11):1223–1232, DOI 10.1080/10255842.2017.1347160, URL https://doi.org/10.1080/10255842.2017.1347160

Bonet J, Wood RD (2008) Nonlinear Continuum Mechanics for Finite Element Analysis, 2nd edn. Cambridge University Press, DOI 10.1017/CBO9780511755446

Chen Y, Medioni G (1992) Object modeling by registration of multiple range images. Image Vision Comput 10:145–155, DOI 10.1109/ROBOT.1991.132043

Chuang JS, Zemljic-Harpf A, Ross RS, Frank LR, McCulloch AD, Omens JH (2010) Determination of three-dimensional ventricular strain distributions in gene-targeted mice using tagged MRI. Magn Reson Med 64(July):1281–1288, DOI 10.1002/mrm.22547

Costandi PN, Frank LR, McCulloch AD, Omens JH (2006) Role of diastolic properties in the transition to failure in a mouse model of cardiac dilatation. Am J Physiol Heart Circ 291(6):H2971–H2979, DOI 10.1152/ajpheart.00571.2006.Role

Finsberg H, Balaban G, Ross S, Håland TF, Odland HH, Sundnes J, Wall S (2018) Estimating cardiac

contraction through high resolution data assimilation of a personalized mechanical model. J Comput Sci 24:85–90, DOI 10.1016/j.jocs.2017.07.013, URL https://doi.org/10.1016/j.jocs.2017.07.013

Hadjicharalambous M, Chabiniok R, Asner L, Sammut E, Wong J, Carr-White G, Lee J, Razavi R, Smith N, Nordsletten D (2014a) Analysis of passive cardiac constitutive laws for parameter estimation using 3D tagged MRI. Biomech Model Mechanobiol pp 807–828, DOI 10.1007/s10237-014-0638-9, URL http://dx.doi.org/10.1007/s10237-014-0638-9

Hadjicharalambous M, Lee J, Smith NP, Nordsletten DA (2014b) A displacement-based finite element formulation for incompressible and nearly-incompressible cardiac mechanics. Comput Methods Appl Mech Eng 274:213–236

Hadjicharalambous M, Asner L, Chabiniok R, Sammut E, Wong J, Peressutti D, Kerfoot E, King A, Lee J, Razavi R, Smith N, Carr-White G, Nordsletten D (2017) Non-invasive Model-Based Assessment of Passive Left-Ventricular Myocardial Stiffness in Healthy Subjects and in Patients with Non-ischemic Dilated Cardiomyopathy. Ann Biomed Eng 45(3):605–618, DOI 10.1007/s10439-016-1721-4, arXiv:1011.1669v3

Holmes JW, Borg TK, Covell JW (2005) Structure and Mechanics of Healing Myocardial Infarcts. Annu Rev Biomed Eng 7(1):223–253, DOI 10.1146/annurev.bioeng.7.060804.100453

Holzapfel GA, Ogden RW (2009) Constitutive modelling of passive myocardium: a structurally based framework for material characterization. Philos Trans Royal Soc A 367:3445–3475, DOI 10.1098/rsta.2009.0091

Kallhovd S, Sundnes J, Wall ST (2019) Sensitivity of stress and strain calculations to passive material parameters in cardiac mechanical models using unloaded geometries. Comput Method Biomec 22(6):664–675, DOI 10.1080/10255842.2019.1579312, URL https://doi.org/10.1080/10255842.2019.1579312

Kerckhoffs RCP, Bovendeerd PHM, Prinzen FW, Smits K, Arts T (2003) Intra- and interventricular asynchrony of electromechanics in the ventricularly paced heart. J Eng Math 47(3-4):201–216, DOI 10.1023/B:ENGI.0000007972.73874.da

Klotz S, Hay I, Dickstein ML, Yi GH, Wang J, Maurer MS, Kass Da, Burkhoff D (2006) Single-beat estimation of end-diastolic pressure-volume relationship: a novel method with potential for noninvasive application. Am J Physiol Heart Circ 291(January 2006):H403–H412, DOI 10.1152/ajpheart.01240.2005

Kolipaka A, Araoz PA, McGee KP, Manduca A, Ehman RL (2010) Magnetic resonance elastography as a method for the assessment of effective myocardial stiffness throughout the cardiac cycle. Magn Reson Med 64(3):862–870, DOI 10.1002/mrm.22467

Krishnamurthy A, Villongco CT, Chuang J, Frank LR, Nigam V, Belezzuoli E, Stark P, Krummen DE, Narayan S, Omens JH, McCulloch AD, Kerckhoffs RCP (2013) Patient-specific models of cardiac biomechanics. J Comput Phys 244:4–21, DOI 10.1016/j.jcp.2012.09.015, URL http://dx.doi.org/10.1016/j.jcp.2012.09.015

Lee J, Cookson A, Roy I, Kerfoot E, Asner L, Vigueras G, Sochi T, Deparis S, Michler C, Smith NP, Nordsletten DA (2016) Multiphysics computational modeling in CHeart. SIAM J Sci Comput 38(3):C150–C178, DOI 10.1137/15M1014097

Nasopoulou A, Shetty A, Lee J, Nordsletten D, Rinaldi CA, Lamata P, Niederer S (2017) Improved identifiability of myocardial material parameters by an energy-based cost function. Biomech Model Mechanobiol 16(3):971–988, DOI 10.1007/s10237-016-0865-3

Nikou A, Dorsey SM, McGarvey JR, Gorman JH, Burdick JA, Pilla JJ, Gorman RC, Wenk JF (2016) Effects of using the unloaded configuration in predicting the in vivo diastolic properties of the heart. Comput Method Biomec 19(16):1714–1720, DOI 10.1080/10255842.2016.1183122, URL http://dx.doi.org/10.1080/10255842.2016.1183122

Nordsletten D, McCormick M, Kilner P, Hunter P, Kay D, Smith N (2011) Fluid-solid coupling for the investigation of diastolic and systolic human left ventricular function. Int J Numer Meth Bio 27:1017–1039, DOI 10.1002/cnm

Peirlinck M, De Beule M, Segers P, Rebelo N (2018) A modular inverse elastostatics approach to resolve the pressure-induced stress state for in vivo imaging based cardiovascular modeling. J Mech Behav Biomed Mater 85(March):124–133, DOI 10.1016/j.jmbbm.2018.05.032, URL https://doi.org/10.1016/j.jmbbm.2018.05.032

Pfaller MR, Hörmann JM, Weigl M, Nagler A, Chabiniok R, Bertoglio C, Wall WA (2019) The importance of the pericardium for cardiac biomechanics: from physiology to computational modeling. Biomech Model Mechanobiol 18(2):503–529, DOI 10.1007/s10237-018-1098-4, URL https://doi.org/10.1007/s10237-018-1098-4, 1810.05451

Rajagopal V (2007) Geometric numerical integration for complex dynamics of tethered spacecraft. Int J Numer Meth Bio (February):1885–1891, DOI 10.1002/nme, 1010.1724

Stoeck CT, Kalinowska A, von Deuster C, Harmer J, Chan RW, Niemann M, Manka R, Atkinson D, Sosnovik DE, Mekkaoui C, Kozerke S (2014) Dual-Phase Cardiac Diffusion Tensor Imaging with Strain Correction. PLoS ONE 9(9):e107159, DOI 10.1371/journal.pone.0107159, URL http://dx.plos.org/10.1371/journal.pone.0107159

Stoeck CT, von Deuster C, Fleischmann T, Lipiski M, Cesarovic N, Kozerke S (2018) Direct comparison of in vivo versus postmortem second-order motion-compensated cardiac diffusion tensor imaging. Magn Reson Med 79(4):2265–2276, DOI 10.1002/mrm.26871

Streeter DD, Spotnitz HM, Patel DP, Ross J, Sonnenblick EH (1969) Fiber orientation in the canine left ventricle during diastole and systole. Circ Res 24(8):339–347, DOI 10.1161/01.RES.24.3.339

Vavourakis V, Papaharilaou Y, Ekaterinaris JA (2011) Coupled fluid and structure interaction hemodynamics in a zero-pressure state corrected arterial geometry. J Biomech 44(13):2453–2460, DOI 10.1016/j.jbiomech.2011.06.024, URL http://dx.doi.org/10.1016/j.jbiomech.2011.06.024

Vavourakis V, Hipwell JH, Hawkes DJ (2016) An Inverse Finite Element u/p-Formulation to Predict the Unloaded State of In Vivo Biological Soft Tissues. Ann Biomed Eng 44(1):187–201, DOI 10.1007/s10439-015-1405-5

Wang ZJ, Wang VY, Babarenda Gamage TP, Rajagopal V, Cao JJ, Nielsen PM, Bradley CP, Young AA, Nash MP (2020) Efficient estimation of load-free left ventricular geometry and passive myocardial properties using principal component analysis. Int J Numer Meth Bio 36(3):1–17, DOI 10.1002/cnm.3313

Xi J, Lamata P, Lee J, Moireau P, Chapelle D, Smith N (2011) Myocardial transversely isotropic material parameter estimation from in-silico measurements based on a reduced-order unscented Kalman filter. J Mech Behav Biomed Mater 4(7):1090–1102, DOI 10.1016/j.jmbbm.2011.03.018, URL http://dx.doi.org/10.1016/j.jmbbm.2011.03.018

Xi J, Lamata P, Niederer S, Land S, Shi W, Zhuang X, Ourselin S, Duckett SG, Shetty AK, Rinaldi CA, Rueckert D, Razavi R, Smith NP (2013) The estimation of patient-specific cardiac diastolic functions from clinical measurements. Med Image Anal 17(2):133–146, DOI 10.1016/j.media.2012.08.001, URL http://dx.doi.org/10.1016/j.media.2012.08.001

Yushkevich Pa, Piven J, Hazlett HC, Smith RG, Ho S, Gee JC, Gerig G (2006) User-guided 3D active contour segmentation of anatomical structures: Significantly improved efficiency and reliability. NeuroImage 31(3):1116–1128, DOI 10.1016/j.neuroimage.2006.01.015

## A Appendix

### A.1 Registration of reference domain to in-vivo images

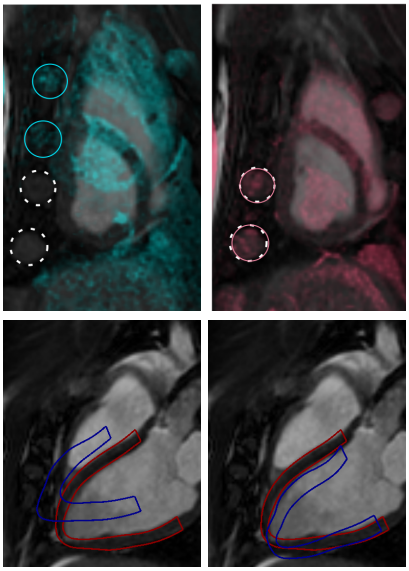

Fig. 8: Top: Reference image (in colour) overlaid on top of the gray-scale ED frame, before (left) and after (right) registration. Circles denote corresponding parts of the ribcage in the reference and in-vivo images, before and after registration. Bottom: Position of the reference mesh (blue) relative to the ED mesh (red), before (left) and after (right) registration.

An essential step was to register the static reference image to the dynamic in-vivo images, in order to determine the relative position between the unloaded domain and in-vivo states. This is a key step for properly simulating the transition from reference domain to in-vivo images and vice-versa and for determining appropriate boundary conditions. However, as there is no known correspondence between the reference domain and a specific frame of the cardiac cycle, use of standard registration for cardiac images would not be possible.

Instead, registration was performed based on non-moving tissues, specifically the ribs. Segmentations of the ribcage in the end-diastolic in-vivo and reference images were used to create surface meshes, which were subsequently registered using the Iterative Closest Point Algorithm (ICP) (Chen and Medioni, 1992) [4]. As the ribcage remains unchanged during the cardiac cycle, any in-vivo frame could had been used instead of the end-diastolic, without affecting the registration result. The resulting transformation information was then used to register the unloaded domain to the in-vivo frames.

[4] Jakob Wilm (2020). Iterative Closest Point (https://www.mathworks.com/matlabcentral/fileexchange/27804-iterative-closest-point), MATLAB Central File Exchange

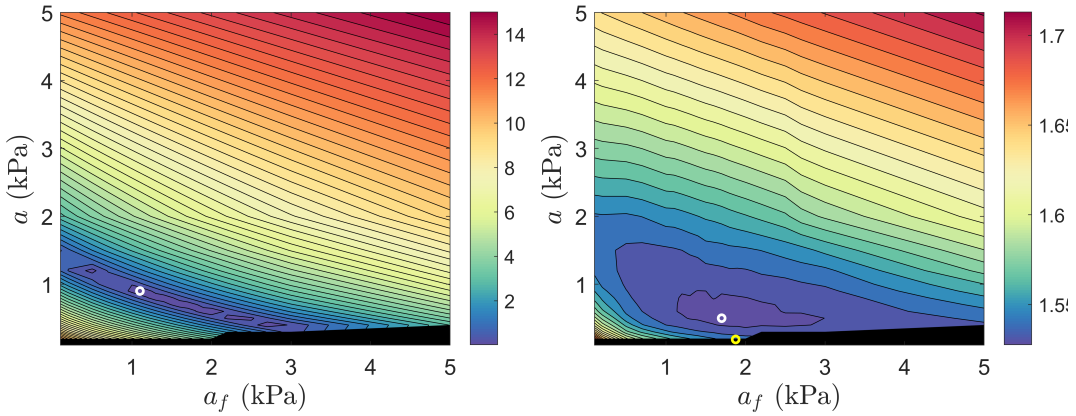


Fig. 9: Behaviour of objective functions relying on cavity volumes (left) and distance (right) metrics, over the parameter space, in inverse simulations. The absolute value of the difference between the simulated cavity volume and $V_{Klotz}$ is presented in mL, while the RMSE between the estimated unloaded domain and the ground-truth reference mesh is given in mm. White circles depict the combination of passive parameters providing the lowest error values, while the yellow circle corresponds to the parameter estimates obtained in the forward simulations' framework.

Figure 8 presents the original misalignment in the ribcage between the reference and in-vivo images, along with its correction after registration.

## A.2 Investigation of passive parameters estimation for inverse model

The joint estimation scheme employed for acquiring passive parameters and reference domain for the inverse model (Sections 4.3.4 and 5.2), relied on matching the cavity volume of the estimated unloaded domain to the Klotz estimate, $V_{Klotz}$. Initially, this was attempted through inverse simulations with sweeps over both passive parameters, with $a$ and $a_f$ varying between $[100, 5000]$. For each combination of passive parameters, the cavity volume of the resulting estimate of the unloaded domain was compared with the Klotz estimate. However, the volume error metric $V_d^{ref}$ exhibited multiple minima over the parameter space (Figure 9), suggesting that is not possible to estimate both passive parameters and unloaded domain through this approach.

To alleviate this issue, the scheme proposed in Section 4.3.4 was performed, whereby the initial estimate of $a_f$ was acquired from the end-systolic model and parameter sweeps were performed only on $a$, leading to the estimates in Table 2. As the choice of $a_f = 1326$Pa was essentially arbitrary, the effect of a different selection for $a_f$ was investigated. Specifically, setting $a_f = 2000$Pa led to $a = 600$Pa and a maximum active tension of $\alpha_{max} = 139$KPa. These estimates are very similar to the values originally estimated for the inverse model ($a = 800$Pa, $\alpha_{max} = 136$KPa), suggesting that the choice of $a_f$ does not have a significant effect on remaining model parameters and model outcomes.

However, an important advantage of this study is that the reference domain is actually available. Accordingly, estimation does not need to rely only on the gross estimate $V_{Klotz}$ but could also take into account the actual geometry of the unloaded state. In this case, parameter estimates of the inverse model were acquired by matching the simulated reference domain to the ground-truth unloaded domain. Estimation was performed by comparing the reference geometries resulting from parameter sweeps with the data-derived reference domain. However, these simulations were run with zero motion applied on the basal boundary, as it was assumed that the relative position between the reference and in-vivo images was not known. Accordingly, the distance errors were calculated after first registering each estimated unloaded geometry to the reference mesh, through point set registration with ICP.

Figure 9 demonstrates the behaviour of the RMSE over the parameter space, which presented a unique minimum. Interestingly, the parameters estimated through this inverse process ($a = 500Pa$, $a_f = 1700Pa$) were not very close to the ground-truth parameters estimated with the forward process ($a = 792Pa$, $a_f = 1200Pa$). This discrepancy in parameters could be attributed to the difference in the boundary conditions employed. Specifically, the ground-truth parameters were obtained with a prescribed motion on the basal plane while inverse parameters were obtained with a fixed base plane.

To further investigate this issue, a separate set of forward simulations employing $\Omega_{REF}$ as the unloaded domain was run. Specifically, following the boundary conditions of the inverse process, LV inflation simulations of the ground-truth reference domain were run with zero displacement enforced weakly on the basal plane. The passive parameter estimates ($a = 187Pa$, $a_f = 1876Pa$) were then obtained using parameter sweeps and ICP registration to the end-diastolic domain, comparing more favourably to the parameters estimated with the inverse process ($a = 500Pa$, $a_f = 1700Pa$), as illustrated with a yellow circle in Figure 9. Interestingly, when employing similar boundary conditions, the forward and inverse simulations lead to similar model outcomes, strengthening the credibility of the modelling framework employed. It is also worth noting that the active tension was not substantially affected by the basal boundary condition in the ground-truth model, giving a maximum value of $\alpha_{max} = 133$KPa for zero basal motion, versus $\alpha_{max} = 125$KPa when displacement was prescribed.